Arabian Journal of Chemistry (2020) 13, 4741–4750

King Saud University

Arabian Journal of Chemistry

www.ksu.edu.sa
www.sciencedirect.com

ORIGINAL ARTICLE

Chitosan coated molybdenum sulphide nanosheet incorporated with tantalum oxide nanomaterials for improving cancer photothermal therapy

Srinivasan Rajasekar [a,*], **Esther Monisha Martin** [a], **Santhi Kuppusamy** [b], **Cittrarasu Vetrivel** [c]

[a] *Kathir Institute of Health Science Wisdom Tree, Neelambur, Coimbatore 641062, Tamil Nadu, India*
[b] *Department of Botany, Selvam Arts and Science College, Namakkal, Tamil Nadu 637003, India*
[c] *Ethnopharmacology and Algal Biotechnology Division, Department of Botany, School of Life Science, Periyar University, Salem 636011, Tamil Nadu, India*

Received 22 August 2019; accepted 17 November 2019
Available online 26 November 2019

KEYWORDS

MoS_2 nanosheet;
Tantalum oxide;
Chitosan;
Cancer photothermal therapy

Abstract In recent years, two-dimensional nanomaterials (2D) prominent for site specific photothermal treatment (PTT), which are one of the most interesting strategy due to their maximizing cancer cell killing efficiency without the normal cells. Several robust methods are established for 2D material synthesis and improving the photothermal conversion efficiency (PCE), biocompatibility, and photostability in cancer PTT. Such preferred mechanism like nanomaterial decoration on to their surface would enable access to tunable 2D nanomaterial properties to improve cancer PTT. Here, we first time report a robust route for deposition of tantalum (TaO_2) on to chitosan (CS) coated molybdenum sulphite (MoS_2) nanosheet surface *via* electrostatic interaction, which assists to improve cancer PTT efficiency. Detailed studies prove that prepared TaO_2-CS-MoS_2 nanomaterial shows lack of toxicity, photostability and PCE was calculated from 26 °C to 47.2 °C under the 808 nm irradiation/5 min. Therefore, the TaO_2 deposition particularly interest to promote the photostability, biocompatibility and PCE of bare MoS_2 nanosheets. Therefore, the possible mechanism is highly expected to improve biological features in cancer PTT.

1. Introduction

Photothermal therapy (PTT) has been realized as a talented route to destroy cancer cells with high efficiency (Nam et al., 2018). This attracted strategy exhibits unique features including low systemic effects, low cost, minimal invasiveness, high selectivity and stability (Khafaji et al., 2019). On the other

* Corresponding author.
E-mail address: sekarbioline@gmail.com (S. Rajasekar).
Peer review under responsibility of King Saud University.

Production and hosting by Elsevier

https://doi.org/10.1016/j.arabjc.2019.11.005
1878-5352

words, well-established PTT agent may enable advances in a precise site-specific heat generator particularly inside the cancer cells under exposure of NIR light, ultrasound, radiofrequency and magnetic field (Cheng et al., 2014). Tremendous number of noble metal isotropic and anisotropic nanoparticles (ANPs) (Alkilany et al., 2012), as well as some 2D materials such as transition metal dichalcogenides (TMDCs), black phosphorous, (Geng et al.,2018) and graphene (Orecchioni et al., 2015) were extensively explored as photothermal conversion agents for cancer PTT. Among them, TMDCs such as MoS_2, WS_2, Bi_2Se_3, TiS_2 and $MoSe_2$ have been widely demonstrated in the cancer PTT. This is because of their unique properties such as owing to their high PCE, good biocompatibility and photothermal stability (Zhang et al., 2017; Li et al., 2018; Shu et al., 2018; Xu et al., 2018). Recently, Molybdenum disulfide (MoS_2) has great attention for PTT due to its remarkable photothermal conversion efficiency (PCE) in the near-infrared (NIR) range and better biocompatibility (Zhang et al., 2018; Liu et al., 2018). Although, most of previous reports has been demonstrated that the modification in the outer or inter-layer sheets of MoS_2 exhibit enhanced PCE with excellent biocompatibility, stability and photothermal conversion efficiency (PCE) (Murugan et al., 2019a,b; Chen et al., 2016). For instance, the surface region of 2D nanomaterial deposition by small sized nanoparticles (NPs) dramatically influenced kupffer cell engulf of 2D materials in vital organs, which in turn helps rapid excretion, increased tumor accumulation and prolonged circulation time in blood (Cheng et al., 2016). Hence, the metal nanostructure decoration on the exterior of MoS_2 suggests a strategy to access new form of 2D materials for cancer PTT. In addition, tantalum oxide (TaO_2) nanoparticles is an ideal material for imaging due to their strong X-ray attenuation as well as combine to PTT agent it can influence the therapeutic ability (Freedman et al., 2014). For example, amalgamation of tantalum oxide (TaO_2) nanoparticles (NPs) into polypyrrole (PPy) NPs improved imaging and photothermal ablation of tumor was estimated to be 66.5% at intravenously injection and 100% for intra-tumoral injection, respectively (Jin et al., 2014). Another report demonstrated that the prepared core/shell nanoparticles using tantalum oxide showed multimodal imaging features including computed tomography (CT), photoacoustic and fluorescence imaging, pH-and thermal-sensitive drug release in cancer therapy (Jin et al., 2017).

Herein, we report the hydrothermal synthesized MoS_2 nanosheet decorated with TaO_2 for cancer PTT. It is a two-step process, wherein MoS_2 nanosheet coated with chitosan (CS) were obtained in the first step and then selectively deposition with TaO_2 in the second step. CS has been widely used as a coated material due to their enhanced biocompatibility enables to get the superior nanomedicine. CS had hydrophilic (—OH) and hydrophobic ($—NH_2$) groups that put forth better degradability, cytocompatibility, and mucoadhesive ability (Fathi et al., 2018). The inherent properties of CS give it an upper hand in terms of promotion of cancer PTT, as well as an effective biopharmaceutical material in cancer applications. The findings revealed that the TaO_2 decorated MoS_2 nanosheets exhibited much better biocompatibility and high PCE. Hence, the surface phase interaction of TaO_2-CS-MoS_2 nanosheet as novel functional material provides a new strategy for cancer PTT.

2. Materials and methods

Sodium molybdate dehydrate ($Na_2MoO_4{\cdot}2H_2O$), thiourea (CH_4N_2S), L-Cysteine, chitosan (CS), tantalum pentoxide (Ta_2O_5), sodium hydroxide (NaOH), hydrochloric acid (HCl). All reagents used as received without any further purification.

2.1. Synthesis of molybdenum disulphide (MoS_2) nanosheet

Hydrothermal route used to fabricate MoS_2 nanosheet at 200 °C for 24 h. In brief, the precursor solution of 50 mg $Na_2MoO_4.2H_20$ mixing with 35 mg of thiourea in 50 mL of deionized water. Then, it was sonicated for 15 min at room temperature and subsequently adjusted to pH 3.5 by adding 0.1 M HCl. Afterward, the reactant was transferred to a teflon-lined autoclave and heated to 200 °C for 18 h in a hot air oven. After completion of the reaction, the black color precipitate was separated from the solution by centrifugation at 8000 rpm for 10 min and washed several times with milliQ water and ethanol to remove any impurities. The black color MoS_2 powder was obtained by drying the precipitate under vacuum at 80 °C overnight (Saada and Bissessur, 2012).

2.2. Synthesis of chitosan coated MoS_2 (CS-MoS_2) nanosheet

In a round bottom flask, 0.3 g of MoS_2nanosheet and 30 mg of L-cysteine was dispersed in 25 mL of milli-Q water under continuous stirring of solution. After 5 h of stirring, 1% CS solution prepared in acetic acid (1%) was added in a drop wise manner at room temperature (RT) to form CS coated MoS_2 nanosheet. After 5 h stirring, the final product was separated by centrifugation and washed with distilled water and ethanol for several times. The resultant nanostructures (CS-MoS_2) were dried overnight under vacuum (Rayappan et al., 2017).

2.3. Synthesis of tantalum oxide materials

For synthesis of TaO_2, 0.05 M of $Ta_2O_5.6H_20$, and 200 μL of 0.5 M NaOH was dissolved in 25 mL of Milli-Q water and the solution was kept overnight under mild stirring. The product obtained was collected by centrifugation and washed several times with milli-Q water and ethanol. The final product was dried at 40 °C for 6 h. After cooling the sample to RT, the powder sample was washed with water for 15 min under ultrasonication and dried under vacuum.

2.4. Synthesis of CS-MoS_2 nanosheet incorporated with TaO_2

Briefly, the concentration of 0.5 mg/mL of as-synthesized TaO_2 and 100 mg of CS-MoS_2 was added in 25 mL of water and the mixture was stirred overnight at RT. Aliquots were collected and purified by repeated centrifugation and washing steps with water and ethanol. The final product (TaO_2-CS-MoS_2) was dried under vacuum and stored for further use.

2.5. Nanomaterials and their characterization

The morphological features and composition of synthesized TaO_2-CS-MoS_2 nanomaterials were observed using transmis-

sion electron microscopy (TEM, JEOL JEM-2100). For X-ray diffraction (XRD) investigations, XRD pattern was recorded on a D/max-2550 PC X-ray diffractometer (XRD; Rigaku, Japan) from 20 to 100°. The structure of TaO_2-CS-MoS_2 nanomaterials was also investigated by Fourier transform infrared (FTIR, Nicolet 6700 Thermo Fisher, USA) spectrometer in the scanning range of 4000–400 cm^{-1}

2.6. Cell line and cell culture condition

The MCF-7 breast cancer cell line was obtained from National Centre for Cell Sciences (NCCS), Pune, India. Then, the cell line was maintained in DMEM media with addition of proper supplements such as 10% (v/v) FBS, 1% (v/v), 100 μg/mL streptomycin and 100 U/mL penicillin. Then, the cells were grown in a humidified incubator at 37 °C under atmosphere supplemented with 95% air and 5% CO_2. The cell culture medium was changed every day, and cells were trypsinized and harvested before reaching confluence.

2.7. Cell viability assay

The HBL-1000 and MCF-7 breast cells were placed in a 96-well plate at a density of 2×10^5 cells/well and grown for 24 h. The grown cells were treated with various concentrations (6, 12, 25, 50, 100 μg/mL) of bare MoS_2, and CS-MoS_2-TaO_2 nanosheets at 37 °C for 24 h. After washing the cells with PBS to remove unbound sheets, 20 μL MTT solution (3-(4, 5-dimethylthiazol-2-yl)-3 2, 5-diphenyltetrazolium bromide) at 0.5 mg mL^{-1} were dropped into the 96-well plate for MTT assay. The cell viability was calculated as a percentage of viable cells after treated with nanomaterials compared with the untreated cells (Murugan et al., 2017).

2.8. Photothermal performance measurement of bare MoS_2 and CS-MoS_2-TaO_2 nanosheets

Photothermal performance experiments of bare MoS_2 nanosheet, and CS-MoS_2-TaO_2 nanosheets were carried out to examine the photothermal conversion efficiency at a laser light source at 808 nm (continuous-wave NIR laser device with power of 0.5 W/cm^2). 0.4 mL of aqueous suspensions containing 100 μg/mL of bare MoS_2 or TaO_2-CS-MoS_2 nanosheets were placed in cuvette and irradiated with 808-nm NIR laser at a power of 0.5 W/cm^2 for 5 min. The temperature increase was monitored for every 30 s using a thermocouple thermometer to determine the PCE of bare MoS_2 and TaO_2-CS-MoS_2 nanosheets.

2.9. Measurement of intracellular ROS generation

To obtain quantitative information about the intracellular free radicals such as peroxide and superoxide free radicals, 5 μg/mL of 2′,7′-Dichlorofluorescein diacetate (DCFH-DA) was added to each well in a 6-well plate containing 4×10^5 cells/well. Samples with final concentration of 200 μg/mL of bare MoS_2 and CS-MoS_2-TaO_2 nanosheets were added to each well and incubated at 37 °C for 24 h in an incubator. The fluorescence intensity of DCF is proportional to the amount of ROS produced by the cell. ROS generation was assessed using a fluorescence microscope (Nikon Eclipse, Inc., Japan) at excitation and emission wavelengths of 488 and 530 nm, respectively (Wang and Cheng, 2019).

For synergistic effects of ROS and PTT assessment, same procedure mentioned above was performed with laser light irradiation at 808 nm for 5 min. After irradiation, the cells were incubated for 24 h, rinsed with PBS, and stained with 20 μM DCFH-DA for 20 min. Subsequently, the fluorescence intensity of DCF in each well was quantitatively estimated by a fluorescence microplate reader.

2.10. In vitro photothermal performance of bare MoS_2 and CS-MoS_2-TaO_2 nanosheets

The MCF-7 cells were incubated in 6-well plates at 37 °C with 5% CO_2 for 24 h. After replacing the medium with pre-warmed new culture medium, bare MoS_2 and 100 μg/mL of CS-MoS_2-TaO_2 nanosheets were added into the wells. After 4 h of incubation, cells were irradiated with 808-nm laser at a power density of 0.5 W/cm^2 for 5 min. The cells were then co-stained with florescent molecules acridine orange (green), propidium iodide (red) and DAPI (blue) investigated in a fluorescent microscope to visualize the structural morphology of live and dead cells. The cell viability was normalized by control group without any treatment.

2.11. Statistical analysis

All the triplicate data were analyzed by student *t*-tests with a setting significance of $p < 0.05$ (*).

3. Results and discussion

The surface decorated 2D nanomaterial by one-dimensional materials offers remarkable physiochemical properties. Hence, various efforts have been devoted to 2D materials to make them highly potential for cancer PTT (Shao et al., 2016; Yi and Zhang, 2018). Herein, we demonstrate the hydrothermal synthesis of MoS_2 nanosheet decorated with TaO_2 for the application of cancer PTT. However, MoS_2 nanosheet decorated with TaO_2 were prepared in two steps: (a) preparation of CS coated MoS_2 nanosheet and (b) decoration with TaO_2. One-pot hydrothermal approach was used to prepare MoS_2 nanosheet using sodium molybdate dehydrate and thiourea as Mo and S source, respectively. As-prepared MoS_2 nanosheet functionalized with cysteine and CS using a disulphite reaction. Afterward, the negatively charged TaO_2 nanoparticles were grafted on the surface of CS-MoS_2 nanosheet, forming TaO_2 decorated MoS_2 nanosheet denoted as TaO_2-CS-MoS_2 nanosheet is illustrated in Scheme 1.

The inclusive shape and layer structural information of the typical MoS_2 nanosheet and TaO_2-CS-MoS_2 were initially determinate by high resolution transmission electron microscopy (HR-TEM) analysis. Based on the profile shown in 1 A, the TEM image revealed monolayer MoS_2 nanosheet exhibit a sheet-like structure with hundreds of nanometers in size. As prepared MoS_2 nanosheet possessed similar sheet-like morphology with previous reports (Yang et al., 2019; Vattikuti et al., 2015). Afterward, the detailed TEM analysis was carried out to confirms the formation of TaO_2-CS-MoS_2 (Fig. 1B). The obtained TEM images clearly shows the small mono-

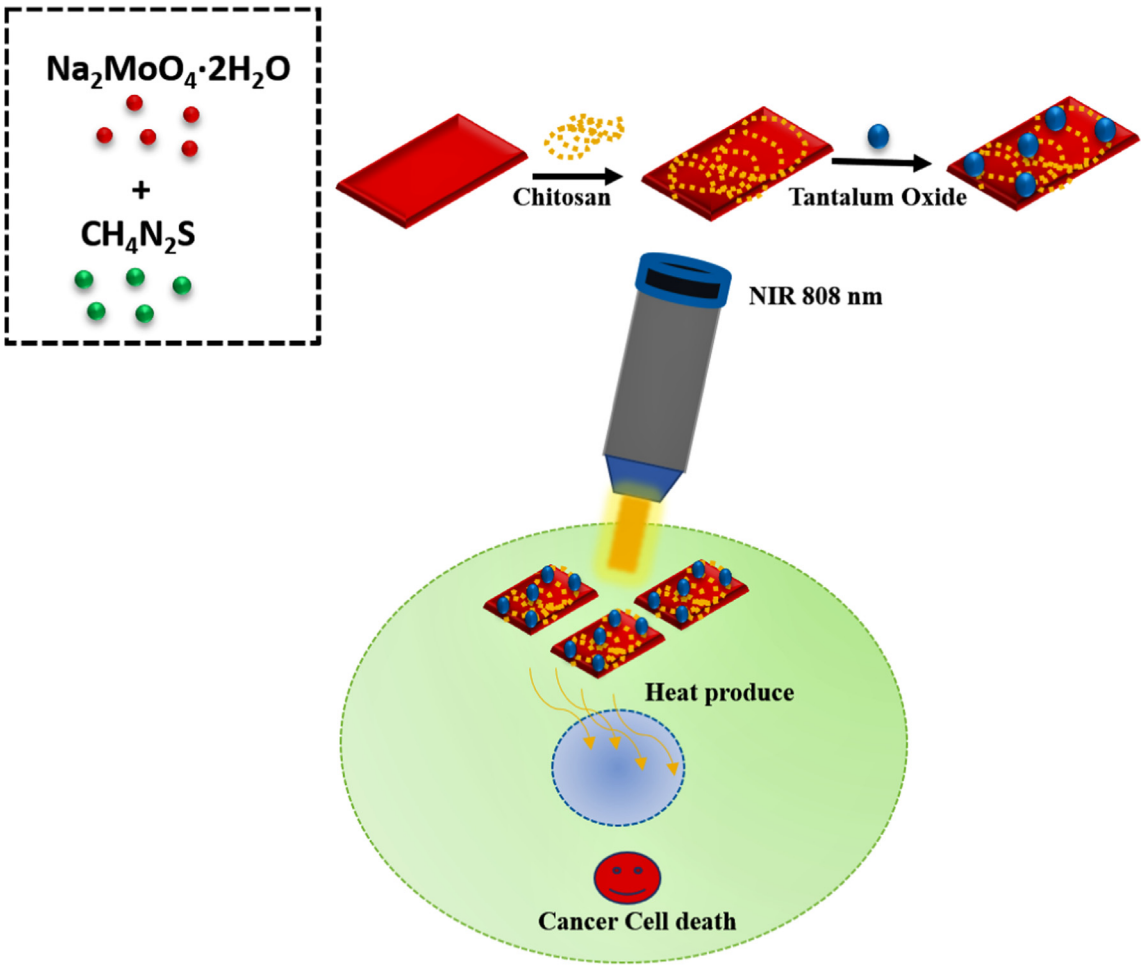

Scheme 1 Schematic representation reveals the fabrication route of TaO_2-CS-MoS_2 nanosheet and their application in cancer PTT.

crystalline hexagonal and semispherical TaO_2 particles with averaged size of 5–10 nm could be found imperfectly onto surface matrix of MoS_2 nanosheet, and thick lucid outer layer around the nanosheet confirms CS coating, describe as CS coated TaO_2-MoS_2 nanosheet. As well as, their HR-TEM cross-sectional images of lattice fringe shown in Fig. 1C. The images reveal that the well stacked with an intrinsic interlayer lattice fringe distance of MoS_2 nanosheets, from which we can assess the averaged interlayer lattice fringes 'd' spacing value was about 0.65 nm, corresponding to the layer aligned with the (0 0 2) basal plane (Mishra et al., 2017). Apart from the fringe, the interlayer lattice 'd' spacing value was estimated to be 0.27 nm, which is representable to the layer aligned with the (1 0 0) lattice plane of MoS_2 nanosheet phase.

As shown in Fig. 2, the small spherical-like TaO_2 nanoparticles were completely covered the inner sheet-like structure of CS-MoS_2 nanosheet.

In addition, UV-NIR spectrum revealed that the broad absorption bands at 320–280 showing that the prepared composite material has CS and tantalum in each exposed surface of sheet-like MoS_2 describes as TaO_2-CS-MoS_2 nanosheet (Fig. 3A). In Fig. 3b shows the crystal structure of sheet-like MoS_2 nanosheet was assessed by the powder X-ray diffraction (XRD) studies that all diffraction peaks can be well indexed and showed at 14°, 32°, and 58° corresponding to the (0 0 2), (1 0 0), and (1 1 0) crystal planes of MoS_2 structure, consistent with the corresponding standard card (JCPDS card number 37-1492) (Qiu et al., 2018). In addition, electron microscopic images of Fig. 3C shows the corresponding selected area electron diffraction (SAED) pattern to the different zone axes of crystallographic orientation in each exposed surface of MoS_2 and TaO_2-CS-MoS_2 nanosheet. In Fig. 3b, the presence of three diffraction rings (1 1 0) (1 0 0) and (0 0 2) reflections corresponding to bare MoS_2 nanosheet conformed by SAED pattern, it further confirming the nature of these nanosheet (Hu et al., 2018). From the Fig. 3D, the electron diffraction collected from TaO_2-CS-MoS_2 ensembles indicates a serious of diffraction peaks related to the TaO_2 lie in the MoS_2 nanosheet plane, the diffraction peaks (white arrows) (1 1 0) (1 0 0) and (0 0 2) reflections corresponding to bare MoS_2 nanosheet, and the presence of the geometric diffraction patterns in the SAED confirms thermally induced crystallization confirms that blending of TaO_2 and MoS_2. It indicates the successfully formation of TaO_2-CS-MoS_2 nanosheet.

The absorption spectrum of TaO_2-CS-MoS_2 shown in Fig. 4A, which showed three absorption bands showing that the prepared composites can strongly absorb the UV light at 280–320 nm. Furthermore, the surface functional groups of bare sheet-like MoS_2, and TaO_2-CS-MoS_2 were evaluated by

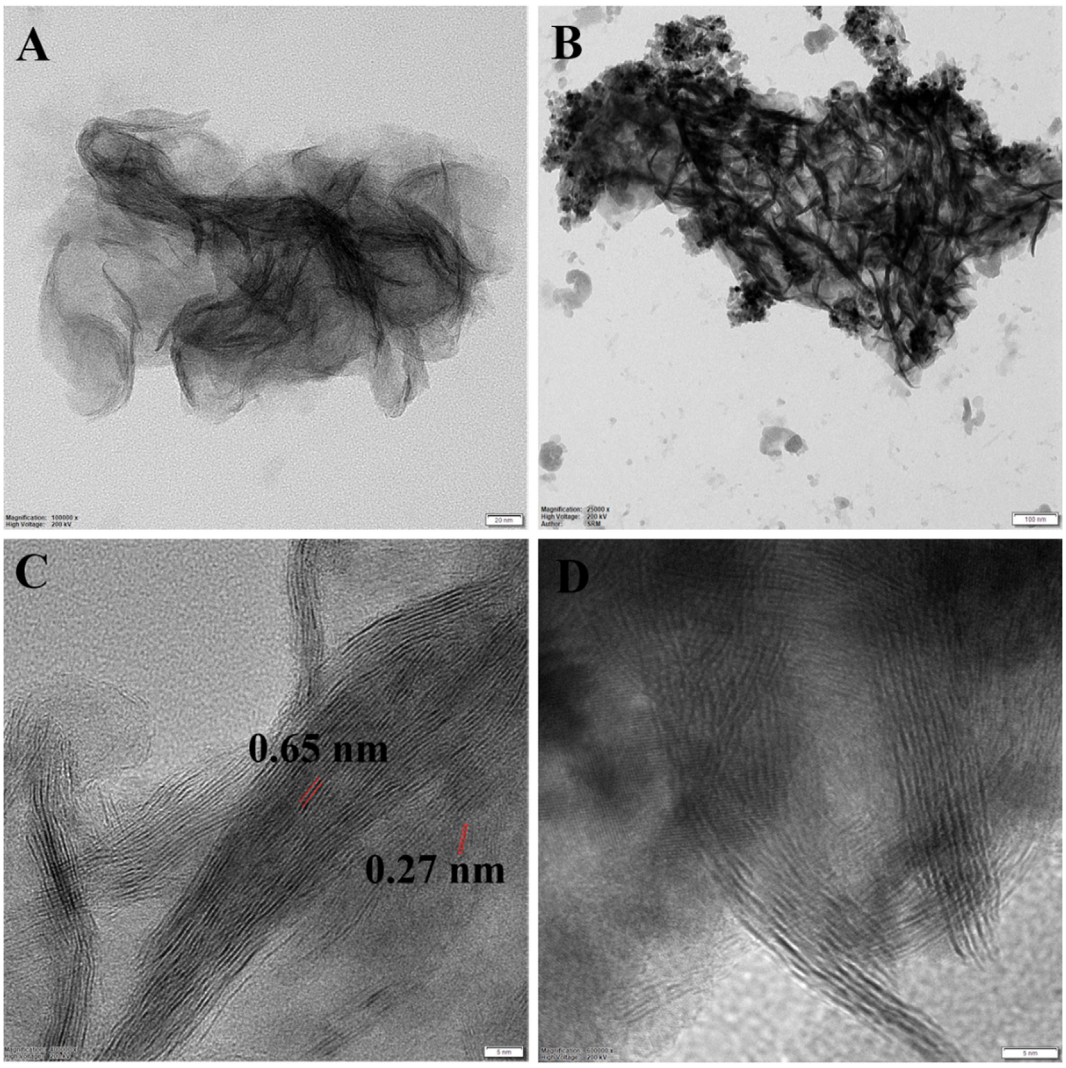

Fig. 1 The morphology and structural features of bare MoS_2 and TaO_2-CS-MoS_2 nanosheet were investigated by electron microscopy. (A & C) TEM image of MoS_2 and (B &D) TaO_2-CS-MoS_2 nanosheet.

FTIR spectra (Fig. 4B). Based on the observation and analyses the FTIR spectrum for bare MoS_2 nanosheet consisting the broad absorption bands at 3416 cm^{-1} formed by the stretching vibration of hydroxyls in the MoS_2 nanosheet. The absorption band between 1100 cm^{-1} and 1650 cm^{-1} is ascribed to the stretching vibrations of the hydroxyl group and Mo-O vibrations, a peak at 900 cm^{-1} represents to the S-S bond. As shown in FTIR spectra of TaO_2 decorated MoS_2 nanosheet, the TaO_2-CS-MoS_2 consisting the major peaks were occurred at 2855, 1100 and 900 cm^{-1} corresponding to MoS_2 and the peaks at 3423, 2356, 539 cm^{-1}, respectively confirmed the presence of TaO_2. The broad absorption bands at 3423 cm^{-1} formed by the stretching vibration of hydroxyls in the TaO_2 and CS, the absorption bands at 1634 cm^{-1} and 1571.05 cm^{-1} are attributed to the presence of the C═O stretching of the amide I band, and bending vibrations of the N—H (N-acetylated residues, amide II band), respectively. It conforms the successfully conjugation of TaO_2 on to the CS-MoS_2 nanosheet to formulate TaO_2-CS-MoS_2 nanosheet.

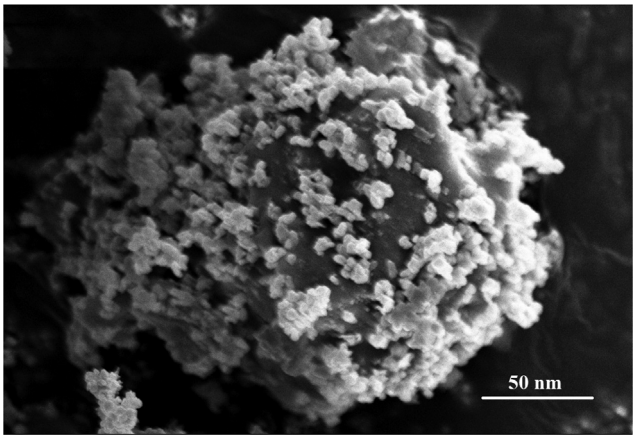

Fig. 2 Scanning electron microscopy (SEM) image reveals the morphology of TaO_2-CS-MoS_2.

MTT assay was performed with human normal cell lines such as HBL-100 to investigate the cyto/biocompatibility of formulated nanosheets. Previous reports demonstrated that the formulated MoS_2 nanomaterials have a significant cytotoxicity for both normal and cancer cell lines. Therefore, MTT

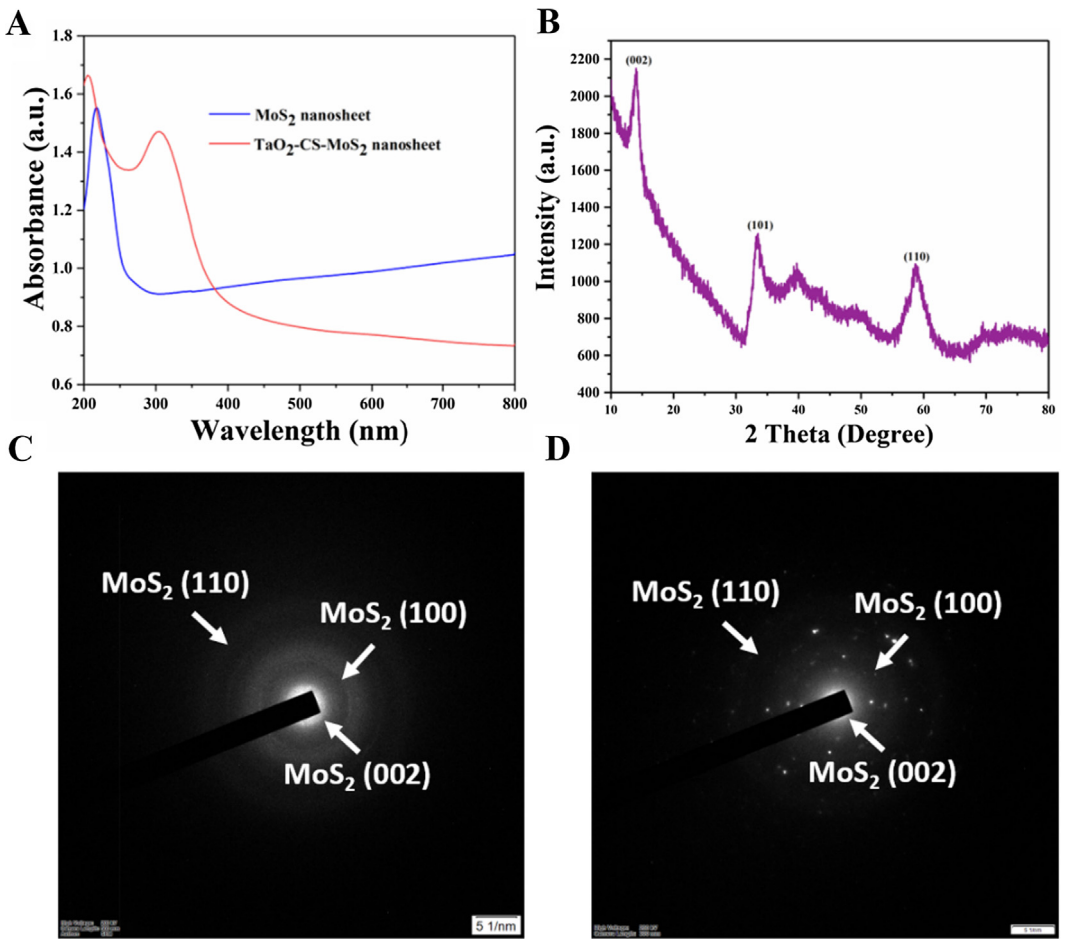

Fig. 3 Physiochemical characteristics of MoS_2 and TaO_2-CS-MoS_2 nanosheet. (A) UV-NIR spectrum of MoS_2 and TaO_2-CS-MoS_2 nanosheet (B) XRD pattern of MoS_2 nanosheet and SAED pattern of (C) bare MoS_2 and (D) TaO_2-CS-MoS_2 nanosheet.

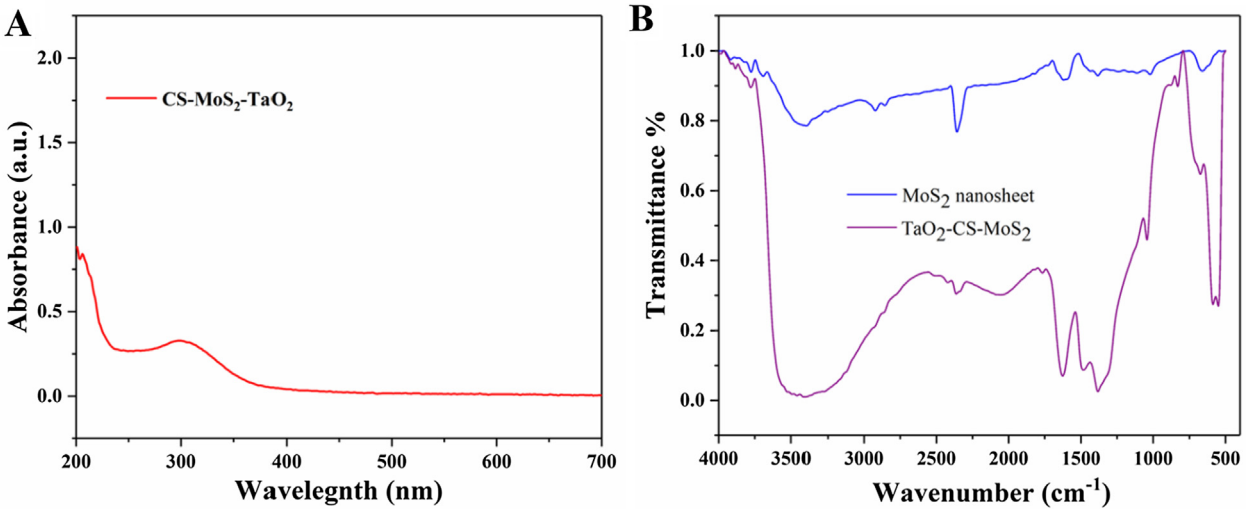

Fig. 4 (A) UV–Vis spectrum of TaO_2-CS-MoS_2 nanosheet and (B) FTIR spectra of MoS_2 and TaO_2-CS-MoS_2 nanosheet.

assay of TaO_2-CS-MoS_2 nanosheets was performed by varying the nanosheets concentrations ranging from 6 to 100 μg/mL for 24 h incubation at 37 °C, as shown in Fig. 5. Even after 24 h of exposure to the highest concentration of nanosheets (100 μg/mL), the viability of the cell population is more than 89.1%, indicating little change in the cell population in the MoS_2 and TaO_2-CS-MoS_2 nanosheet treating HBL-100 cells. Notably, the increase of TaO_2-CS-MoS_2 concentration

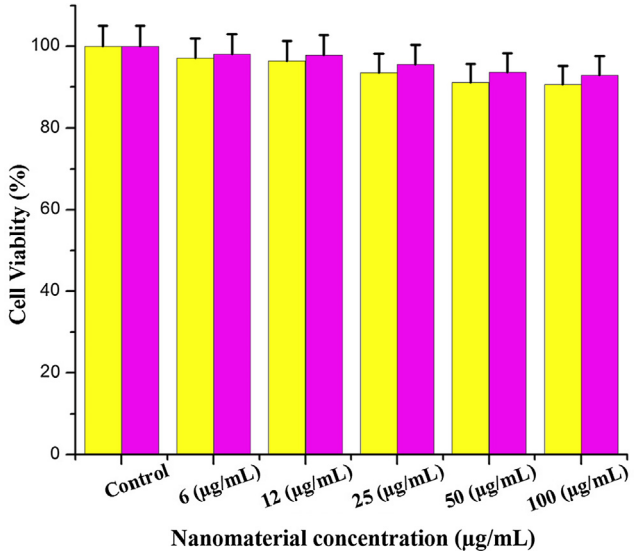

Fig. 5 Evaluation of cell viability by MTT assay. The HBL-100 normal breast cells were treated with different nano-formulations at various concentration (6–100 µg/mL) for 24 h at 37 °C.

enhances the viability of cells indicating that biocompatibility nature (Gao et al., 2016).

The photothermal performance of bare MoS_2 and TaO_2-CS-MoS_2 nanosheet (at concentration of 50 and100 µg/mL) in 0.4 mL water at irradiating the suspension with laser light of 808 nm at a power density of 0.5 W/cm^2 for 5 min was performed. The temperature was monitored as a function of time, Fig. 6A. Afterwards, the temperature of suspension containing nanosheet modified with TaO_2 increased from room temperature of 26 to 42.7 and 47.6 °C, at concentration of 50 and 100 µg/mL of TaO_2-CS-MoS_2, respectively. The rate of heat generation was higher in the initial period of 2–3 min. It is worth noting that nanosheets prepared with TaO_2 improve the heat generation and rise the temperature as about 47.5 °C at 100 µg/mL concentration of TaO_2-CS-MoS_2 concentration. Similar experiments with bare MoS_2 nanosheets and pure milli-Q water showed a temperature increase of only 38.5 °C and 27.8 °C from RT, indicating that TaO_2 decoration significantly improves PCE of MoS_2 nanosheets at lower power density (0.5 W/cm^2). It indicated that TaO_2 decoration happened to be on the surface of sheet petals, which in turn, influences the photon absorption ability of MoS_2 nanosheets. Heating and cooling cycles of 100 µg/mL of TaO_2-CS-MoS_2 were monitored continuously for 5 cycles to investigate their potential (photothermal stability) for cancer PTT (Fig. 6B and C). There was no change in heat generation ability of TaO_2 decorated nanosheets. Notably, the PCE of nanosheet was maintained at 47.6% at 100 µg/mL of TaO_2-CS-MoS_2. Such materials have great potential as photothermal agents in cancer PTT as it can easily induce thermal damage to the targeted tissues by increasing the local temperature to >42 °C (hyperthermia) (Chen et al., 2014a,b).

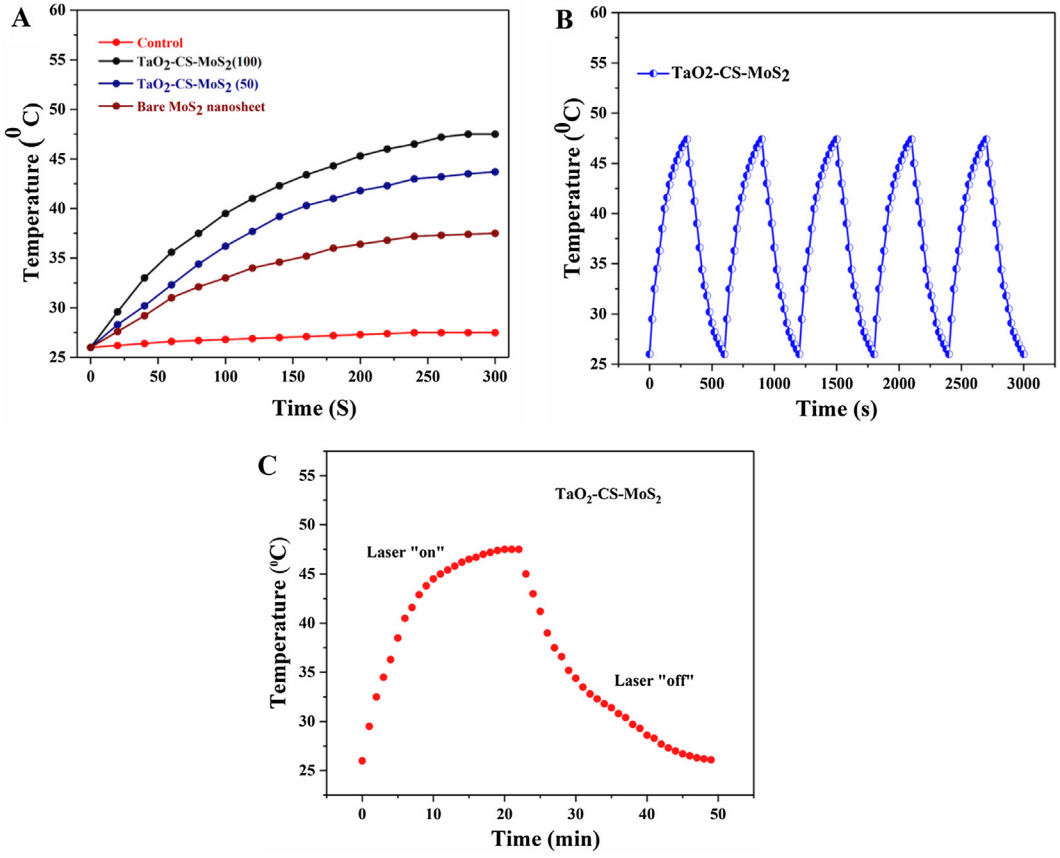

Fig. 6 *In vitro* photothermal-property characterization of TaO_2-CS-MoS_2 nanosheet. (A) The photothermal-heating curves and (B and C) repeated heating–cooling profiles of different concentrations of TaO_2-CS-MoS_2 nanosheet in an aqueous solution after 808 nm laser irradiation at 0.5 W/cm^{-2} for five laser on/off cycles.

To get more detailed information about PTT induced cytotoxicity for MCF-7 cells, MTT assay and apoptosis staining techniques were performed TaO_2-CS-MoS_2 under laser irradiation at 808 nm for 5 min. Red fluorescent intensity was highly occurred in the cells were treated with TaO_2-CS-MoS_2 nanosheet, which indicates the treatment effectiveness of TaO_2 decorated materials (Fig. 7A). The DAPI staining proved the fragmentation of nuclear segments after the irradiation with TaO_2-CS-MoS_2 nanosheet (Fig. 7B). Notably, the cell viability was deduced for TaO_2-CS-MoS_2 nanosheet at 100 μg/mL concentration, when compared to control cells (cells irradiated with laser light), as shown in Fig. 7C. Thus, TaO_2-CS-MoS_2 nanosheets shown the excellent cytotoxicity against cancer cells under laser light irradiation. It is worth noting that direct irradiation of the MCF-7 cells without nanosheet as a control does not affect the cell viability. It indi-

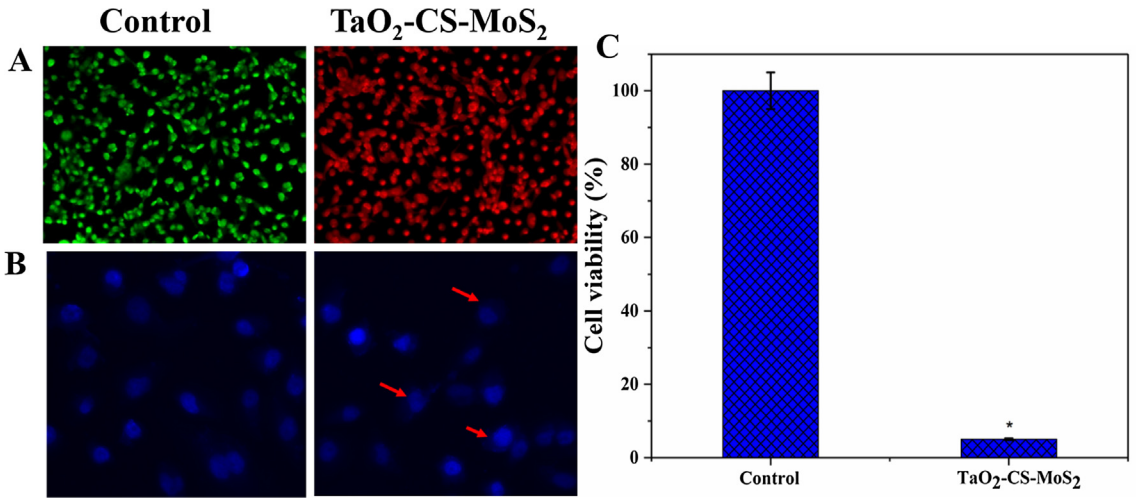

Fig. 7 (A) Fluorescent microscopic images of MCF-7 cells staining with acridine orange (green) and propidium iodide (red) after irradiation with 808 nm laser light for 5 min and (B) DAPI (blue) staining and (C) the cell viability was assessed by MTT assay.

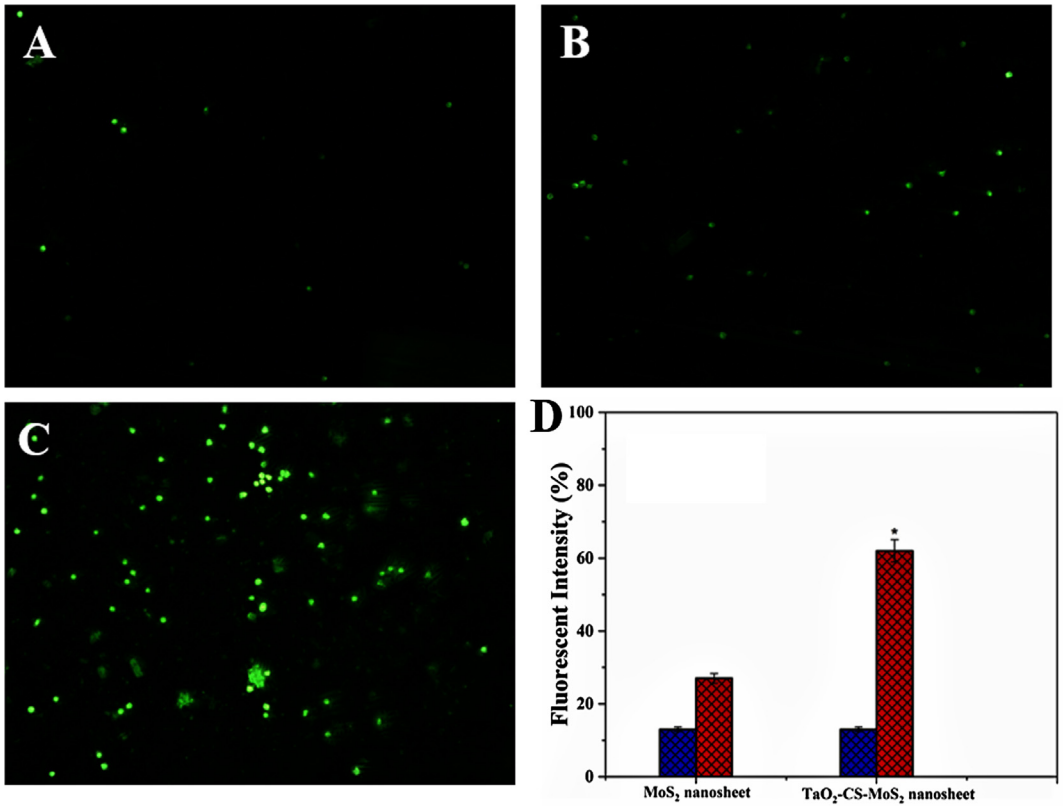

Fig. 8 ROS production in DCFH-DA stained MCF-7 cells incubated with MoS_2 and TaO_2-CS-MoS_2 nanosheets with or without laser treatment at 808 nm for 5 min (10× magnification).

cated that TaO_2 decoration influence the photon absorption ability of MoS_2 nanosheet (Chen et al., 2014a,b).

ROS generation was studied in the MCF-7 cells treating with bare MoS_2 and TaO_2-CS-MoS_2 nanosheets at a higher concentration (100 μg/mL) for 24 h. After treated, the cells were stained with dichloro-dihydro-fluorescein diacetate (DCFH-DA) to examine ROS generation. (Fig. 8A–C). On the contrary, the fluorescence intensity improved as a function TaO_2 concentration in MCF-7 cells indicating the rise of ROS production. ROS intensity was analyzed by fluorescence plate reader (Fig. 8D) in both normal and breast cancer cells after the treating with bare MoS_2 and TaO_2-CS-MoS_2 nanosheets. Notably, the higher fluorescence intensity was observed for MCF-7 cells treated with TaO_2-CS-MoS_2 nanosheets when compared to bare MoS_2 nanosheets. The increased levels of ROS mediated cancer cell death were clearly pointed out in TaO_2-CS-MoS_2 nanosheet treated MCF-7 breast cancer cells. It proves TaO_2 decoration on to MoS_2 nanosheet plays a key role in activating intrinsic apoptotic signaling pathways in MCF-7 cancer cells influences ROS generation during the PTT therapy (Murugan et al., 2016; Thapa et al., 2018; Gao et al., 2019).

4. Conclusion

In summary, we demonstrated the effects of ultra-small sized TaO_2 decoration onto the surface of MoS_2 nanosheet, in which, the increased concentration of TaO_2-CS-MoS_2 nanosheet increase the cell viability nature of MoS_2 nanosheet in normal HBL-100 breast cells. It indicates TaO_2 decoration on to the surface of MoS_2 significantly improve the biocompatibility, photo conversion effects, photostability and remarkable photothermal therapeutic effects then bare MoS_2 nanosheets. This work opens a new avenue to tune the physio-chemical properties of 2D nanomaterials by metal decoration.

Declaration of Competing Interest

The authors declared that there is no conflict of interest.

References

Alkilany, A.M., Thompson, L.B., Boulos, S.P., Sisco, P.N., Murphy, C.J., 2012. Gold nanorods: their potential for photothermal therapeutics and drug delivery, tempered by the complexity of their biological interactions. Adv. Drug Deliv. Rev. 64 (2), 190–199.

Chen, Q., Wang, C., Zhan, Z., He, W., Cheng, Z., Li, Y., Liu, Z., 2014a. Near-infrared dye bound albumin with separated imaging and therapy wavelength channels for imaging-guided photothermal therapy. Biomaterials 35 (28), 8206–8214.

Chen, J., Wang, X., Chen, T., 2014b. Facile and green reduction of covalently PEGylated nanographene oxide via a 'water-only'route for high-efficiency photothermal therapy. Nanoscale Res. Lett. 9 (1), 86.

Chen, Y., Wang, L., Shi, J., 2016. Two-dimensional non-carbonaceous materials-enabled efficient photothermal cancer therapy. Nano Today 11 (3), 292–308.

Cheng, L., Wang, C., Feng, L., Yang, K., Liu, Z., 2014. Functional nanomaterials for phototherapies of cancer. Chem. Rev. 114 (21), 10869–10939.

Cheng, L., Shen, S., Shi, S., Yi, Y., Wang, X., Song, G., Yang, K., Liu, G., Barnhart, T.E., Cai, W., Liu, Z., 2016. $FeSe_2$-decorated Bi_2Se_3 nanosheets fabricated via cation exchange for chelator-free 64Cu-labeling and multimodal image-guided photothermal-radiation therapy. Adv. Funct. Mater. 26 (13), 2185–2197.

Fathi, M., Majidi, S., Zangabad, P.S., Barar, J., Erfan-Niya, H., Omidi, Y., 2018. Chitosan-based multifunctional nanomedicines and theranostics for targeted therapy of cancer. Med. Res. Rev. 38 (6), 2110–2136.

Freedman, J.D., Lusic, H., Snyder, B.D., Grinstaff, M.W., 2014. Tantalum oxide nanoparticles for the imaging of articular cartilage using X-ray computed tomography: visualization of ex vivo/in vivo murine tibia and ex vivo human index finger cartilage. Angew. Chem. 53, 8406–8410.

Gao, F., He, G., Yin, H., Chen, J., Liu, Y., Lan, C., Zhang, S., Yang, B., 2019. Titania-coated 2D gold nanoplates as nanoagents for synergistic photothermal/sonodynamic therapy in the second near-infrared window. Nanoscale 11 (5), 2374–2384.

Gao, S., Zhang, L., Wang, G., Yang, K., Chen, M., Tian, R., Ma, Q., Zhu, L., 2016. Hybrid graphene/Au activatable theranostic agent for multimodalities imaging guided enhanced photothermal therapy. Biomaterials 79, 36–45.

Geng, B., Yang, D., Pan, D., Wang, L., Zheng, F., Shen, W., Zhang, C., Li, X., 2018. NIR-responsive carbon dots for efficient photothermal cancer therapy at low power densities. Carbon 134, 153–162.

Hu, J.J., Cheng, Y.J., Zhang, X.Z., 2018. Recent advances in nanomaterials for enhanced photothermal therapy of tumors. Nanoscale 10 (48), 22657–22672.

Jin, Y., Li, Y., Ma, X., Zha, Z., Shi, L., Tian, J., Dai, Z., 2014. Encapsulating tantalum oxide into polypyrrole nanoparticles for X-ray CT/photoacoustic bimodal imaging-guided photothermal ablation of cancer. Biomaterials 35 (22), 5795–5804.

Jin, Y., Ma, X., Zhang, S., Meng, H., Xu, M., Yang, X., Xu, W., Tian, J., 2017. A tantalum oxide-based core/shell nanoparticle for triple-modality image-guided chemo-thermal synergetic therapy of esophageal carcinoma. Cancer Lett. 397, 61–71.

Khafaji, M., Zamani, M., Golizadeh, M., Bavi, O., 2019. Inorganic nanomaterials for chemo/photothermal therapy: a promising horizon on effective cancer treatment. Biophys. Rev., 1–18

Li, B., Gu, P., Zhang, G., Lu, Y., Huang, K., Xue, H., Pang, H., 2018. Ultrathin nanosheet assembled $Sn_{0.91}Co_{0.19}S_2$ nanocages with exposed (100) facets for high-performance lithium-ion batteries. Small 14 (5), 1702184.

Liu, Y., Peng, J., Wang, S., Xu, M., Gao, M., Xia, T., Weng, J., Xu, A., Liu, S., 2018. Molybdenum disulfide/graphene oxide nanocomposites show favorable lung targeting and enhanced drug loading/tumor-killing efficacy with improved biocompatibility. NPG Asia Mater. 10 (1), e458.

Mishra, R., Nirala, N.R., Pandey, R.K., Ojha, R.P., Prakash, R., 2017. Homogenous dispersion of MoS_2 nanosheets in polyindole matrix at air-water interface assisted by Langmuir technique. Langmuir 33 (47), 13572–13580.

Murugan, C., Rayappan, K., Thangam, R., Bhanumathi, R., Shanthi, K., Vivek, R., Thirumurugan, R., Bhattacharyya, A., Sivasubramanian, S., Gunasekaran, P., Kannan, S., 2016. Combinatorial nanocarrier based drug delivery approach for amalgamation of anti-tumor agents in breast cancer cells: An improved nanomedicine strategy. Sci. Rep. 6, 34053.

Murugan, C., Venkatesan, S., Kannan, S., 2017. Cancer therapeutic Proficiency of dual-targeted mesoporous silica nanocomposite endorses combination drug delivery. ACS Omega 2 (11), 7959–7975.

Murugan, C., Murugan, N., Sundramoorthy, A.K., Anandhakumar, S., 2019b. Nanoceria decorated flower-like molybdenum sulphide nanoflakes: an efficient nanozyme to tumour selective ROS generation and photo thermal therapy. Chem. Commun. 55, 8017–8020.

Murugan, C., Sharma, V., Murugan, R.K., Malaimegu, G., Sundaramurthy, A., 2019a. Two-dimensional cancer theranostic nanomaterials: synthesis, surface functionalization and applications in photothermal therapy. J. Control. Release 299, 1–20.

Nam, J., Son, S., Ochyl, L.J., Kuai, R., Schwendeman, A., Moon, J.J., 2018. Chemo-photothermal therapy combination elicits anti-tumor immunity against advanced metastatic cancer. Nature Commun. 9 (1), 1074.

Orecchioni, M., Cabizza, R., Bianco, A., Delogu, L.G., 2015. Graphene as cancer theranostic tool: progress and future challenges. Theranostics 5 (7), 710.

Qiu, M., Wang, D., Liang, W., Liu, L., Zhang, Y., Chen, X., Sang, D. K., Xing, C., Li, Z., Dong, B., Xing, F., 2018. Novel concept of the smart NIR-light–controlled drug release of black phosphorus nanostructure for cancer therapy. Proc. Natl. Acad. Sci. 115 (3), 501–506.

Rayappan, K., Murugan, C., Sundarraj, S., Lara, R.P., Kannan, S., 2017. Peptide-conjugated nano-drug delivery system to improve synergistic molecular chemotherapy for colon carcinoma. ChemistrySelect 2 (27), 8524–8534.

Saada, I., Bissessur, R., 2012. Nanocomposite materials based on chitosan and molybdenum disulfide. J. Mater. Sci. 47 (15), 5861–5866.

Shao, J., Xie, H., Huang, H., Li, Z., Sun, Z., Xu, Y., Xiao, Q., Yu, X. F., Zhao, Y., Zhang, H., Wang, H., 2016. Biodegradable black phosphorus-based nanospheres for in vivo photothermal cancer therapy. Nat. Commun. 7, 12967.

Shu, Y., Li, B., Chen, J., Xu, Q., Pang, H., Hu, X., 2018. Facile synthesis of ultrathin nickel–cobalt phosphate 2D nanosheets with enhanced electrocatalytic activity for glucose oxidation. ACS Appl. Mater. Interfaces 10 (3), 2360–2367.

Thapa, R.K., Soe, Z.C., Ou, W., Poudel, K., Jeong, J.H., Jin, S.G., Ku, S.K., Choi, H.G., Lee, Y.M., Yong, C.S., Kim, J.O., 2018. Palladium nanoparticle-decorated 2-D graphene oxide for effective photodynamic and photothermal therapy of prostate solid tumors. Colloids Surf., B 169, 429–437.

Vattikuti, S.P., Byon, C., Reddy, C.V., Venkatesh, B., Shim, J., 2015. Synthesis and structural characterization of MoS_2 nanospheres and nanosheets using solvothermal method. J. Mater. Sci. 50 (14), 5024–5038.

Wang, X., Cheng, L., 2019. Multifunctional two-dimensional nanocomposites for photothermal-based combined cancer therapy. Nanoscale.

Xu, Y., Li, B., Zheng, S., Wu, P., Zhan, J., Xue, H., Xu, Q., Pang, H., 2018. Ultrathin two-dimensional cobalt–organic framework nanosheets for high-performance electrocatalytic oxygen evolution. J. Mater. Chem. A 6 (44), 22070–22076.

Yang, L., Zhang, J., Feng, C., Xu, G., Xie, C., Yuan, X., Xiang, B., 2019. MoS2 nanosheet/MoS_2 flake homostructures for efficient electrocatalytic hydrogen evolution. Mater. Res. Express 6 (8), 085005.

Yi, M., Zhang, C., 2018. The synthesis of two-dimensional MoS 2 nanosheets with enhanced tribological properties as oil additives. RSC Adv. 8 (17), 9564–9573.

Zhang, A., Li, A., Zhao, W., Liu, J., 2017. Recent advances in functional polymer decorated two-dimensional transition-metal dichalcogenides nanomaterials for chemo-photothermal therapy. Chem. – Eur. J. 24 (17), 4215–4227.

Zhang, X., Xiao, S., Nan, H., Mo, H., Wan, X., Gu, X., Ostrikov, K. K., 2018. Controllable one-step growth of bilayer MoS_2–WS_2/WS_2 heterostructures by chemical vapor deposition. Nanotechnology 29 (45), 455707.